Preparation, structural characteristics and optical parameters of the synthesized nano-crystalline sulphur doped $Bi_2Te_{2.85}Se_{0.15}$ thermoelectric materials

M.S. Shalaby[1,*], H.M. Hashem[2,*], N.M. Yousif[1], H.A. Zayed[3], A. Sotelo[4], L.A. Wahab[1]

[1]Thermal and Magnetic Lab., Solid-State Physics and Accelerators department, National Center for Radiation Research and Technology, Atomic Energy Authority, B.O. Box 29 Nasr City, Cairo, Egypt.

[2]Physics Department, Faculty of Science, Helwan University, 11798 Helwan- Cairo, Egypt.

[3]Ain Shams University, Faculty of women for Art Sciences and Education, Heliopois, Cairo, Egypt

[4]Instituto de Ciencia de Materiales de Aragón (ICMA), CSIC-Universidad de Zaragoza, Maria de Luna, 3, 50018 Zaragoza, Spain

Abstract

In the present work, a systematic preparation of $Bi_2Te_{2.85}Se_{0.15-x}S_x$ (x=0.0, 0.02, 0.04 and 0.06) compositions were carried out by solvothermal method. The materials were characterized by XRD, SEM, EDX, TEM and Raman spectroscopy.XRD, as well as TEM, to confirm the nanostructure of samples. The electrical and thermal properties were investigated in the temperature range from room temperature to 600 K. The highest power factor was 1.3 x 10^{-2} mW/ K^2 m at 600 K for (x=0.06) sample. This improvement in the thermoelectric properties may be due to the ordered atomic arrangement of Bi, Te, and Se induced by sulphur in the $Bi_2Te_{2.85}Se_{0.15-x}S_x$ nano-composites, which was confirmed by X-ray diffraction (XRD) and Raman spectral analysis. The optical properties, such as energy gap, refractive index, extinction coefficient and dielectric constants, were obtained from the diffused reflectance data in the range of 200 to 800 nm. Sulphur doping influences the optical energy gap, reaching the lowest value for x=0.04 samples (0.14 eV), while the highest allowed energy gap was found in x=0.06 ones (0.41eV).

***Keywords*:** Solvothermal method, $Bi_2Te_{2.85}Se_{0.15}$, XRD, SEM, TEM, Electronic thermal conductivity, power Factor, optical energy gap, dielectric constants.

*Corresponding authors:
M.S. Shalaby, Thermal and Magnetic Lab., Solid-State Physics and Accelerators department, National Center for Radiation Research and Technology, Atomic Energy Authority, B.O. Box 29 Nasr City, Cairo, Egypt. E-mail:phymshalaby@gmail.com, Tel:+2 01112289938
H.M. Hashem, Physics Department, Faculty of Science, Helwan University, 11798 Helwan- Cairo, Egypt. E-mail:hany_m_hashem@yahoo.com, Tel:+2 01096743169

1. *Introduction:*

Typically the energy costs have been increased all around the world, and turned out to be one of the most important issues for society. Also, the growing energy demand has led to energetic crises in many nations around the world. With all the accessibility of the enormous amount of energy that comes from the sun (heat and light), there is a huge interest in harvesting this solar-powered energy. The two main ways of harvesting this particular solar-powered energy and transform it into electricity are i) photovoltaic (PV) cells; and ii) Solar thermal heat engines [1-4]. Specifically, solar power (thermal) provides a huge potential for development either by producing efficient selective surfaces to be able to collect the concentrate the heat of the sunlight or by making use of an auxiliary device in order to increase the overall performance of the solar energy plant using thermoelectric generators (TEG's) [5-7]. However, several studies have been carried out on the production of high-electric power devices for micro-electromechanical systems (MEMS), portable and wearable electronics [8]. As a result, the current trend is concerned on bulk and thin film nano-structured thermoelectric devices [9,10]. The band gap is also considered an important aspect of thermoelectric materials and defines the characteristics of thermoelectric materials, such as the Seebeck coefficient, as well as, electrical conductivity [11].

The simple expression found for the efficiency can be employed by using the average values of these material properties for any range of interest in temperature [12-16].

The efficiency of thermoelectric (TE) materials is defined by the dimensionless thermoelectric figure of merit, ZT, which is given by [17];

$$ZT = \frac{s^2 \sigma \ T}{k} \qquad (1)$$

where, $\boldsymbol{\sigma}$ is the electrical conductivity, $\boldsymbol{k}$ the thermal conductivity, $\boldsymbol{S}$ the Seebeck coefficient and $\boldsymbol{T}$ the absolute temperature.

In order to obtain TE materials with high ZT and efficiencies, the power factor ($\boldsymbol{S^2\,\sigma}$) should be maximized, while minimizing thermal conductivity [18, 19]. The recent progress in these materials is due to the possibility of enhancing the TE materials and devices efficiency at nano-scale through different approaches. Semiconductor compounds like bismuth telluride (Bi_2Te_3) and other chalcogenides are gaining attention for use in thermoelectric devices and photoconductive materials because of their high TE performance [20-22]. However, the need of materials with adequate stability at high temperatures in the presence of high humidity has led to the search for new, and more efficient materials [23]. Many researchers have been working to fabricate doped Bi_2Te_3 nanoparticles as well as nanocomposites [7, 24-26]. However, to enhance phonon scattering, nanostructuring is desirable because it creates random interfaces on a nanometer scale, reducing the mean free path of phonons, leading to an effective reduction in lattice thermal conductivity. Moreover, they enhance the thermoelectric performance, and produce significant microstructural modifications in the bulk thermoelectric matrix. These nanostructures can be fabricated through different techniques [27, 28, 29]. As a result of these previous works, it has been found that n-type $Bi_2Te_{2.85}Se_{0.15}$ has excellent thermoelectric properties [27, 28]. However, the production of n-type $Bi_2Te_{2.85}Se_{0.15}$ with high thermoelectric properties requires the addition of harmful halide dopants [30-32]. To date, various kinds of dopants were investigated, such as Fe, Mn, I, Sn, O, Ce, Y, Sm and S [29, 33]. These $Bi_2Te_3(Se_3)$ doped materials are promising in a large variety of applications like solid state coolers, thermal energy harvesting, diluted magnetic semiconductors, magneto-resistance switches and topological insulators. Most recently, sulphur substitution/doping has shown a major effect in reducing lattice thermal conductivity of nanoporous Bi_2Te_3 polycrystals, with values in the $0.3 \leq \kappa_L \leq 0.6\ W\,m^{-1}\,K^{-1}$ range, which can be related to modifications in the charge carriers mobility, as well as, on electron scattering [34]. According to the previous work, sulphur doping modifies band gap, defect localized states, lattice distortions, and energy levels [35]. Hence, not only the type of dopants is influencing properties, but also their distribution and the effect in the host material are critical and very sensitive for their electronic structures, optical and thermal properties. Bismuth-based thin film compounds were studied before as well as used in many optical and thermoelectric devices because the variation in band gap of thermoelectric materials has a significant effect on the Seebeck coefficient and the electrical conductivity [36,37].

In this study, sulphur doping effect on the morphology, and microstructure, as well as thermoelectric and optical properties of the $Bi_2Te_{2.85}Se_{0.15}$ system will be studied. Moreover, in order to produce nanostructured compounds, the solvothermal method will be used due to its simplicity.

On the other hand, sulphur atoms distribution and the lattice distortion in S-doped $Bi_2Te_{2.85}Se_{0.15}$ will be determined by X-ray diffraction (XRD), Energy Dispersive X-ray (EDAX) and Raman Spectroscopy. Surface morphology will be studied through Scanning Electron Microscopy (SEM), as well as High-

resolution Transmission Electron Microscopy (TEM). Moreover, electrical resistivity, Seebeck coefficient, electronic thermal conductivity, and optical properties, such as the band gap, dielectric constants and refractive index for the nanostructure prepared materials will be also determined and related to the structural and microstructural modifications.

2. Experimental Details

2.1 Preparation of $Bi_2Te_{2.85}Se_{0.15-x}S_x$

$Bi_2Te_{2.85}Se_{0.15-x}S_x$ (x=0.0, 0.02, 0.04 and 0.06) nanopowders were prepared using the solvothermal method. A mixture of $BiCl_3$ (10 mmol), Te, Se and S powders with high purity (99.99%) (15 mmol) and KOH (80 mmol) were mixed into a 100 ml capacity graded beaker to prepare the precursors S-doped $Bi_2Te_{2.85}Se_{0.15}$ precursors. Then, sodium borohydride, $NaBH_4$ (30 mmol), was added as organic complexing reagent. N-N dimethylformamide (DMF) solvent was added to the mixture into the beaker up to 90ml, and heated into a muffle furnace at 150°C for 24 hours, followed by gradual cooling down to room temperature. The obtained dark-gray powders were washed with double distilled water and filtered several times to remove any residual precursors or by-products, followed by drying in a vacuum oven at 85°C for 14 hours. Finally, agglomerates were crushed by manual milling using an agate mortar, leading to very fine powders.

2.2 Measurement techniques:

Energy-Dispersive X-ray spectrometer (EDX) BRUKER Nano GmbH D-12489, 410-M unit (Berlin-Germany) was employed to investigate and determine the elemental composition of the prepared samples by using mapping method. This unit was used combined with scanning electron microscopy (SEM), which has been used to observe the surface morphology of specimens. X-ray diffractometer, Shimadzu XRD-6000, with Cu K_α radiation λ=1.54056 Å, 2θ-step of 0.02º from 4º to 80º, has been used to determine the structure of the samples. In order to confirm the chemical structures of $Bi_2Te_{2.85}Se_{0.15}$, including doping, a Raman spectrometer Labram HR Evolution, with Argon ion laser at 514 nm at room temperature has been utilized. High-resolution transmission electron microscopy (HRTEM) images were obtained by using (HRTEM, Jem-2100, Jeol, Japan). Thermoelectric power measurements were made stablishing temperature differences along the length of the specimen by heating one end utilizing of an auxiliary heater and keeping the other colder. The temperature gradient (ΔT) has been measured using two thermocouples in an evacuated chamber. Besides, the electromotive force dE (or thermovoltage ΔV) has been measured at each lead of the thermocouples. From each ΔT and ΔV measurement data, Seebeck coefficient can then be easily calculated according to ($S = {}^{\Delta V}/_{\Delta T}$). The electrical resistivity (or conductivity) was measured by using the DC four-point probe technique, where a constant current (I) is generated into the rod sample by two electrodes. The resulting potential drop (V) was also measured by the thermocouples wires. So, finally, electrical resistivity can be easily calculated from the relation ($\rho = \frac{V}{I}\frac{A}{L}$ and $\sigma = \frac{1}{\rho}$). Moreover, Seebeck coefficient and electrical conductivity (or resistivity) of bulk materials were simultaneously measured using a Linseis LSR-3 under He atmosphere.
The optical energy gap, refractive index and the other optical properties of the samples were investigated from diffused reflectance which measured from (λ=200-1200 nm) by Fourier transform infrared (UV-VIS) spectrometer (NICOLET iS10 model instrument).

3. Computing and Programming:

3.1. Lattice parameters calculations :

UnitCell software has been used to refine lattice parameters and unit cell volume from powder diffraction data. It utilizes a non-linear least squares method, which allows carrying out the refinement on the observed X-ray powder diffraction data.

3.2. Winfit program

Rietveld refinement of the obtained XRD patterns was performed using Winfit software, to make a deconvolution of the samples diffractograms. Additionally, it was utilized for crystallites size and strains calculations.

3.3. Raman fitting Data

PeakFit is a computerized nonlinear pinnacle detachment and examination programming bundle for researchers performing spectroscopy, chromatography and electrophoresis. It allows finding and fitting up to 100 peaks to an informational index, at any given moment, empowering users to portray pinnacles and locate the best conditions to accommodate their data. PeakFit can likewise improve the information acquired from customary numerical techniques and lab instruments.

4. Results and Discussions:

4.1. Energy-dispersive X-ray spectroscopy (EDX):

EDX spectra for $Bi_2Te_{2.85}Se_{0.15-x}S_x$ (x=0.0, 0.02, 0.04 and 0.06) compositions are depicted in ***Figure 1***. The EDX and elemental mapping spectra indicated that all samples besides the expected Bi, Te, Se and S elements, contain C and O as foreign elements, which can be due from traces in the sample holder or from reactants. It has been found that S peaks intensity increases when the dopant content is raised. Also, the intensity of the Bi and Te/Se ratios was indeed influenced by the sulphur doping which resulted from the redistribution of Bi and Te elements during the phase development.

4.2. SEM Imaging:

Figure 2 shows SEM images and elemental mapping of $Bi_2Te_{2.85}Se_{0.15}$ composition. From SEM images, it can be observed that grains are irregular, randomly oriented, and relatively small, in the order of a hundred nanometers. However, very large particles are also visible in the background of the image. Besides, it can be observed that particle size also varies depending on the S-doping concentration. This effect is due to the fact that sulphur can change the bonds strength as well as the bond order, modifying the growth rates along *a, b and c* axis. Moreover, it has been found in all samples that always there are a few tiny grains among the larger ones, showing a significant non-uniformity. This microstructure may be responsible for a significantly larger phonon scattering, but may not disperse most of the charge carriers [38,39].

4.3. X-ray diffraction (XRD):

The X-ray diffraction patterns of $Bi_2Te_{2.85}Se_{0.15-x}S_x$ (x=0.0, 0.02, 0.04 and 0.06) are depicted in ***Figure 3***. Phase identification shows that the samples are mainly Bi_2Te_3 (JCPDS 45-0863) single phase materials with very small Se content. They have been indexed according to a rhombohedral system (Space group R*3m*), and their structural dimensions/features are given in ***Table 1***.
The obtained XRD data have been fitted using Winfit program. The profile fitting plots are illustrated in ***Figure 4*** for the highest intensity peaks. The deconvolution data obtained from Winfit program were used in computing grain size and the strains shown in ***Table 1***. Moreover, ***Table 1*** lists the lattice parameters, which have been obtained from Unitcell program.
There are two potential factors behind the discrepancy between SEM imaging and the XRD data in grain size computations: i) the resolution of the SEM is limited and cannot capture the littlest particles as the XRD could do. ii) Individual particles may have agglomerated, then some of these agglomerates can be observed through SEM as an individual particle. Consequently, TEM has been used to confirm the presence of nanocrystals, as XRD has determined.
The results showed that the grain sizes were in the ≈ 20 nm range. Furthermore, the unit cell volume was increased when S concentration increases, even though the ionic radius of S = 0.184 nm is smaller than that of Se = 0.194 nm [40], as depicted in ***Figure 5***. In order to understand this behavior, two possibilities have to be considered. Firstly, the unit cell volume might be affected by crystalline deffects like: i) atomic scale point defects like antisite defects (Bi'_{Te} and Bi'_{Se}) and donor-like defects ($V_{Te}^{\bullet\bullet}$ and $V_{Se}^{\bullet\bullet}$). ii) Antisite defects may occur during the crystal growth or the donor-like defects appear during the hand-grinding. iii) Crystalline imperfections like the dislocations developed during the deformation process [35]. Secondly, electro-negativity of S (2.44 Pauling units) is lower than that of Se (2.48 Pauling units) [41], and may reduce the bond order and increase the bonding length. According to the obtained data, the unit cell volume is increased when S doping concentration is raised, as illustrated

in ***Figure 5***, which makes the second mechanism more reasonable for explaining this behaviour. It is clear that sulphur doping in Se/Te site plays an important role in the phase formation due to the nature of the bonds between the Bi-Te (covalent or mixed ionic and covalent bonds) and Te-Te (weak Van der Waals bonds) [42]. So, through the different preparation steps, $Bi_2Te_{2.85}Se_{0.15-x}S_x$ crystals grow forming small plate-like grains, which would be in thermodynamic equilibrium while they are metastable due to their high surface energy [43,44]. As the reaction process continued, large amount of small and active centers may exist, which could provide many high energy sites for nanocrystal grow. In addition, due to the anisotropic nature of Bi_2Te_3 that may be reflected in an anisotropic grain growth, leading to the formation of nanoplates [44].

4.4. HRTEM imaging

Figure 6 shows the TEM images for the $Bi_2Te_{2.85}Se_{0.11}S_{0.04}$ powdered samples. The $Bi_2Te_{2.85}Se_{0.11}S_{0.04}$ images show the formation of plate–like nanograins after sintering procedure. ***Figure 6a*** shows that these nanoplates, with different sizes, appear clearly agglomerated in HRTEM images. Moreover, their edges in the basal facets are not well defined. These nanoparticles sizes vary from 40 to 82 nm for the large structures and from 5 to 20 nm for the smaller ones, as depicted in ***Figure 6b***, which is a beneficial microstructure for thermoelectric materials. These data clearly confirm that the particle sizes of the samples are typically in the nano scale as previously deduced from XRD patterns. The control of the morphology was proposed to be affected by the preparation method and the possible mechanisms of the Bi_2Te_3 nanoplates with different shapes and dimensions as well [45-47]. Hee-Jin Kim et al., proposed that the usage of the surfactant, reaction temperature and the addition of $NaBH_4$ may vary and control the morphology [48]. Also, these factors could preferentially induce the growth of the doped $Bi_2Te_{2.85}Se_{0.15}$ crystals along *the ab plane* during the nucleation step. On the other hand, the particles shape reflects the strong connection (covalent /ionic bond) between Bi-Te, and the weak bond (Van der Waals) between Te-Te layers, as previously mentioned [42,49]. Furthermore, Te-Se or Te-S may lead to larger distortions, slippage of the grains and producing defects

4.5. Raman Spectroscopy:

Raman microspectroscopy and imaging Raman microscopy offer unique opportunities for studying the evolution and spatial distribution of chemical phases in ceramic semiconductors. It proved to be a convenient strategy to study the elementary excitations and their interactions in material sciences. ***Figure 7*** shows the Raman spectrograms recorded for sulphur-doped samples. It is clear that the fundamental vibrational modes of Bi_2Te_3 are located at wave numbers about 122 cm^{-1}, 134 cm^{-1} and 758 cm^{-1} in agreement with the literature [50]. Raman spectra of $Bi_2Te_{2.85}Se_{0.15-x}S_x$ samples were fitted and decomposed into individual Gaussian components to obtain the natural frequency of each Raman mode. The fitted spectra are depicted in ***Supplementary Data. Table 2*** shows the Raman modes of $Bi_2Te_{2.85}Se_{0.15-x}S_x$ samples of the current study compared with previous data for Bi_2Te_3 compounds. In the figure, three prominent peaks are observed, which correspond to E^2g, A^1u and A^1g modes at low wave numbers. The A^1u mode for Bi_2Te_3 appears just in low dimensional structures as a consequence of the symmetry breaking in Bi_2Te_3 [51]. A blue shift occurred within the Raman frequency as the reduction in the dimensions, due to the changes in the materials vibrational attributes [51]. Usually, in the nanostructure, the volume compression may arise from the size-induced radial pressure, which increases in the force constants. As the sulphur-doping concentration increases all Raman modes soften linearly and expand, as shown in ***Figure 8***, due to the fact that Raman shift and full width at half maximum (FWHM) are controlled by phonon anharmonicity. In the nanostructures, the shift in the Raman peak can be more easily recognized than FWHM, because the FWHM is extremely affected by changes in the focus of the laser beam and the laser spot position. Besides, as sulphur in the nanostructures can be found in the Se site, we especially focused on the surface phonon mode SPM peak shift [52] which is only observed in nanosized materials at 95 cm^{-1}. The decrease of the superficial force constant in nanosized crystals can lead to an increase in the inter-atomic distance in surface layers than in bulk samples. Thus, this surface phonon mode has a lower frequency than E^2_g, while both of them have similar behavior. Meanwhile, the Raman shift of this mode changes when S concentrations increase. Interestingly, nanostructured Bi_2Te_3 displays an extra peak at ≈120 cm^{-1} not detected in the bulk phase, confirming the data from XRD as well as TEM. This mode was identified as an A^1_u mode (X peak) observed in nano-crystalline and few-quintuple thick Bi_2Te_3 [53]. It is significant that the A^1_u mode originated as an active phonon mode in the infrared (IR) is forbidden in Raman for centro-symmetric Bi_2Te_3 [50,54,55], where the existence of Te1 atoms in the center of Bi_2Te_3 unit cell makes the IR active modes (A^1_u) to be odd parity. As the polarizability of odd parity modes does not change,

they are often inactive modes for Raman, especially in centro-symmetric molecules [53]. It is worth noting that, A^1_u mode appears in our samples with low-dimensional structure which may break the centro-symmetric nature of Bi_2Te_3 (due to defects). It is well-known that defects in nanostructures (such as vacancies of Bi, antisite, maybe Te excess, etc.) play a very important role in lifting symmetry-based selection rules. On the other hand, the Te spectrum demonstrates a strong Raman peak at about 118/120 cm^{-1} wavenumber. It should be noted that the spectra of few monolayer Bi_2Te_3 show lines at ~ 93 cm^{-1} and 114 cm^{-1}, and they may be attributed to the Se and S doping, as previously mentioned [50, 52,54,55]. Furthermore, samples with S=0.00 and S=0.06 clearly exhibit a lower shoulder (≈115 cm^{-1}) in the A^1_u mode (due to excess of Te as compared to Bi_2Te_3) leading to A^1_u peak broadening. The peak at ≈90 cm^{-1} (SPM) is observed in the Raman spectra for all the nanostructured Bi−Te specimens below the E_g^2 mode. This information, obtained from Raman spectroscopy, fits very well with XRD and TEM data, showing that the prepared samples are in the nano scale with no doubt. Interestingly, The Raman peaks/shifts were found to be very sensitive to both the crystal orientation and the polarization configuration. Indeed, a weak Raman peak at ≈200cm^{-1} in the spectra (signed in our samples 172: 185 cm^{-1}) can be attributed to the expected B^1_g (sulphur) phonon modes. The peak at 756 cm^{-1} is an overtone of the A^2_{1g} mode [56].

4.6. ***Thermoelectric Properties:***

4.6.1. Seebeck coefficient:

The Seebeck coefficient measures a voltage difference resulting from a temperature difference throughout the thermoelectric material. This is the opposite of the Peltier effect, which is the creation of hot and/or cold zones due to the flowing of current through a conductor. The Seebeck coefficient (*S*) versus temperature for the $Bi_2Te_{2.85}Se_{0.15}S_{0.15-x}$ (x=0.0, 0.02, 0.04 and 0.06) samples with different sulphur ratios is depicted in ***Figure 9***. The negative values of the Seebeck coefficient are a shred of evidence that the majority carriers are electrons (n-type). The $Bi_2Te_{2.85}Se_{0.15}$ had the maximum absolute Seebeck coefficient, i.e., **-108 µV/K** at **600 K**. On the other hand, the values for the sulphur-doped samples are lower than for the undoped ones ($Bi_2Te_{2.85}Se_{0.15}$), which prove the effect of sulphur doping on both the structure and thermal properties. Also, the increase in Sulphur, together with the reduction of Te concentration in the matrix might result in a decrease in the Seebeck coefficient as previously mentioned [57], as confirmed from EDAX ***Figure 1***. This decrease in Seebeck coefficient with the decrease in Se content confirms the increase in carrier concentration due to the inverse relationship between Seebeck coefficient and carrier concentration. The non-monotonic variation of the Seebeck coefficient was caused by the bipolar effect that may take place when both n and p types carriers are present [58].

4.6.2. Electrical resistivity measurements:

The dependence of electrical resistivity with temperature has been simultaneously obtained with the Seebeck coefficient. In ***Figure 10***, it can be clearly seen that the electrical resistivity decreases when the temperature increases for all samples, which is the expected behavior for a non-degenerate semiconductor. It is known that the resistivity is very sensitive to microstructural variations, specifically to the grain sizes and lattice imperfections in solids (such as vacancies and dislocations). In these samples, there is a slight difference in grain sizes between the S un-doped/doped samples. Even though the largest grain sizes are found in $Bi_2Te_{2.85}Se_{0.11}S_{0.04}$, the increase in its electrical resistivity values up to 500K may be due to the effect of the surface scattering rather than the grain boundaries scattering according to Samble's previous studies [59,60]. Furthermore, Devries made an interpretation about this criterion showing that the electrons at a lower distance from the surface than the mean free path, could be scattered at the surface [61]. It means that the effect of surface scattering would be more effective than that of the grain boundaries scattering since the electrons will have to pass through the grains independently of temperature. On the other hand, $Bi_2Te_{2.85}Se_{0.11}S_{0.04}$ samples showed the lowest Seebeck coefficient between the sulphur-doped samples. So, it is suggested that the decrease in Se content plays an important role in the formation of a fine-grained microstructure, hence resulting in increasing carriers scattering and thus electrical resistivity, especially with higher concentrations of sulphur. However, the carrier concentrations increase indeed when the resistivity decreases according to the relation [62]:

$$\sigma = 1/\rho = n\, e\, \mu = \frac{ne^2\tau}{m^*} \qquad (2)$$

According to the equation, the increase in carrier concentration (n) and mobility (μ) reduce electrical resistivity. On other hand, sulphur may be randomly distributed and influences the carriers mobility and the resistivity as well. Also, it has been mentioned before that S-doping affects the bond order and so does on the chemical bonds that can significantly influence the carrier mobility which agrees with previous obtained data from XRD [63,49,64].

4.6.3. Power factor (PF):

Figure 11 shows the temperature dependence of power factor of $Bi_2Te_{2.85}Se_{0.15}S_{0.15-x}$ (x=0.0, 0.02, 0.04 and 0.06) samples. It is expressed as [65]:

$$\boldsymbol{PF = \sigma S^2 = \frac{S^2}{\rho}} \qquad (3)$$

Typically PF can be improved by increasing the Seebeck coefficient and electrical conductivity. In the figure, it can be observed that power factor increases gradually when the temperature is raised for all samples reaching the highest values at the highest temperatures. Even though Seebeck coefficient is high for the undoped samples, its PF is smaller than x=0.02 samples due to its lower electrical resistivity. Consequently, it is easy to deduce that electrical resistivity is the most important parameter in these samples. The highest PF values have been reached in $Bi_2Te_{2.85}Se_{0.13}S_{0.02}$ samples in the whole measured temperature range, up to 1.3 x 10^{-2} mW/ K^2m at 600 K. When compared to the undoped $Bi_2Te_{2.85}Se_{0.15}$ samples prepared before at different temperatures, both undoped as well as the doped samples have opposite behavior to that mentioned [30]. Also, the values in this study for the power factor were lower than the reported in [30,66] at 330K, while at 600K the values are higher than the obtained in n-type $Bi_2Te_{2.85}Se_{0.15}$ single crystals or in previously reported materials [64, 30, 66].

4.5.4 Electronic Thermal conductivity

Thermal conductivity of semiconductors can be approximately estimated from the equation, $\kappa = \kappa_{el} + \kappa_{ph}$ [67], where κ_{el} and κ_{ph} represent carrier and phonon contributions to thermal conductivity, respectively. In the direct band gap semiconductors, the electronic part (κ_{el}) is dominant over the phonons (κ_{ph}) contributions. The particular carrier-related thermal conductivity κ_{el} can be computed from the electrical resistivity (ρ) according to the Wiedemann–Franz law: $\kappa_{el} = LT/\rho$ [67], where L is the Lorentz constant ($1.5x10^{-8}$ V^2/K^2) for nearly degenerate semiconductors [68,69]. ***Figure 12*** shows the calculated electronic thermal conductivity for sulphur-doped $Bi_2Te_{0.85}Se_{0.15}$. From the above discussion, it appears that the electrical resistivity decreases with increasing temperature, so the carrier concentration increases as mentioned before in Eq. (2), resulting in an increase in carrier-related thermal conductivity κ_{el}. On the other hand, ***Figure 12*** shows remarkable information: firstly, the highest recorded value for the electronic thermal conductivity was $1.4x10^{-2}$ W/m K for $Bi_2Te_{0.85}Se_{0.09}S_{0.06}$ samples at 600 K. Secondly, the electronic thermal conductivity for the Sulphur-doped samples increases gradually more than in the $Bi_2Te_{0.85}Se_{0.15}$ samples, especially at higher temperatures. This effect can be ascribed to the anisotropy in the crystal structure and the orientation of the grains due to the sulphur-doping. Also, this effect may be attributed to electron scattering from sulphur dopant sites [34]. Thirdly, it is very remarkable that the values of electronic thermal conductivity were smaller than the values achieved before in refs. [34,70].

4.6 Optical Properties of $Bi_2Te_{0.85}Se_{0.15-x}S_x$
4.6.1. Band gap

Figure 13 shows the different diffused reflectance spectra of $Bi_2Te_{0.85}Se_{0.15-x}S_x$ samples from 200 to 800 nm. The reflectance peaks were determined with λ=210 nm for all samples. It can be seen that x=0.04 samples have large reflectance values on all wavelength range. The optical absorption coefficient α of samples with various wavelengths was estimated according to Kubelka-Munk relation [71]:

$$F(R) = \frac{(1-R)^2}{2R} \qquad (4)$$

Where, F(R) is the function of Kubelka-Munk, which is related to the absorbance and R is the diffused reflectance. $\boldsymbol{\alpha}$ is the linear absorption coefficient which could be evaluated from F(R) values from the following relation [72,73] :

$$\alpha = \frac{F(R)}{t} = \frac{\text{Absorbance}}{t} \qquad (5)$$

Where, t is the sample thickness. The dependence of **α** on **hυ** relation used by Tauc and Menth's to calculate the optical band gap energy as well as the type of transition [74, 75].

$$(\alpha h\upsilon) = \frac{F(R)h\upsilon}{t} = A(h\upsilon - E_g)^m \qquad (6)$$

Where, E_g is the band gap energy, hυ is the energy of the photon, and A is a proportionality constant which depends on the transition probability and is associated with the effective masses related to the bands. The exponent (m) depends on the nature of the transition (m= 2 for direct and 1/2 for indirect semiconductor).

Figure 14 shows the plotted relation between $(\alpha h\upsilon)^{1/2}$ against the energy (hυ) for all samples. The optical energy gap is obtained by extrapolating the linear portion of the curve to the energy axis. All the plots show straight-line portions supporting the interpretation of the indirect band gap for all the powder samples. The energy gap values were increased when S doping is increased except for x=0.04, which shows the lowest energy gap value as tabulated in a table (1). This may be occurred due to many reasons such as the existence of defects [76], the increase in the grain size or the decrease in the strains [77]. All these parameters confirm the previous data obtained from the structural analysis (XRD). The obtained data were very close to that data obtained before by Akrap et al. for Se doped Bi_2Te_3 crystals and seems to be in agreement with result in [78]. It has been reported in [79,80] that the electronegativity difference of the doping elements may be attributed to the lone pair p-orbital related to chalcogenide atoms (Te, Se) as well as to the variation in the values of the energy gap. Accordingly, the substitution of low electronegative elements in the site of high electronegative ones increases the energy of some lone pair states, broadening the valence band in the forbidden gap, leading to band tailing as well as shrinking the band gap. But in this work, the results point out to the opposite behavior, although S electronegativity is lower than Se one, as mentioned in XRD data, and the increase of the energy gap generally for undoped x=0(0.23 ev), x=0.02(0.33ev) and x= 0.06(0.41ev) may due to the difference between them in their grains, lattice parameters and the strain [76,77].

4.6.2. *The refractive index dispersion*

The refractive index is a vital tool to obtain the packing density, the chemical bonding and the electronic structure of the material [81,82]. The refractive index (n) as well as the extinction coefficient (K) was evaluated from the obtained data. For this purpose, M. Caglar et al. relations were used [83]:

$$R = \frac{(n-1)^2+K^2}{(n+1)^2+K^2} \qquad (6)$$

$$n = \frac{(1+R)}{(1-R)} + \sqrt{\frac{4R}{(1-R)^2} - K^2} \qquad (7)$$

$$K = \frac{\alpha\lambda}{4\pi} \qquad (8)$$

Where, R is the reflectance. The refractive index (n) and the extinction coefficient (K) dependence on the wavelength (λ) at different sulphur concentrations are shown in ***Figures 15*** and ***16***, respectively. It clearly appears that the refractive index sharply decreases when the wavelength increases up to 210 nm, then a very strong peak appears at 230 nm, drastically decreasing for all samples up to the highest wavelength. It is remarkable that sulphur doping attributed the n values drastically due to it is a smaller ionic radius than that of Se. Also, it is studied before that the larger ionic radius of the atom, the larger will be its polarizability. But here from XRD data, it was shown that there are some traces from Se appearing as minor phases, which affect the S/Se relationship. On the other hand, there were some studies evaluating the dependence of the refractive index on the Se content on thin films, and explained by Lorentz–Lorenz formula, showing a direct proportion between the polarizability and refractive index [79, 80, 84]. As there are relative differences between the ionic radii of Bi, Te, Se and S, the replacement between more polarized atoms with less ones, the refractive index increases in these studies. Whereas in our case, the less polarized S atom replaces the more polarized Se, therefore, the refraction index is decreasing for the S=0.02 and 0.06 samples, while the S=0.04 the highest values due to its highest content of Se minor phase, as mentioned in XRD. It means that incomplete phase

transformation as well as the presence of quantum size effect originated by the microstructure nature and S/Se ratio.

Figure 16 shows the relationship between the extinction coefficient (K) and wavelength (λ). All the curves exhibit a peak at 210 nm due to the change in the absorption. Then, the extinction coefficient increases monotonically with the increase of wavelength. This increase in K with λ can be associated with the portion of light absorbed in the samples at higher λ. On the other hand, according to [85,86], in the case of the diffused reflectance, the values of the extinction coefficient are very small for the powder material and that appears clearly in ***Figure 16***. So, the equations 7, and 8 can be rewritten as:

$$R = \frac{(n-1)^2}{(n+1)^2} \quad (9)$$

$$n = \frac{(1+R)}{(1-R)} + \sqrt{\frac{4R}{(1-R)^2}} \quad (10)$$

4.6.3. *Dielectric constants*

The complex dielectric constant is composed of two parts, the real (ε_r) and the imaginary (ε_i), as shown in the following expressions [87]:

$$\varepsilon^* = \varepsilon_r + i\varepsilon_i \quad (11)$$

where,

$$\varepsilon_r = n^2 - k^2 \quad (12)$$

$$\varepsilon_i = 2nk \quad (13)$$

The variation of both parts of the dielectric constant (ε_r & ε_i) with the wavelength are depicted in ***Figure 17***, where it can be observed that their values are affected by their relation with n as well as K. So their curves show the same behavior observed in n and K as well. So, it is clear from ***Figure 17*** that the real dielectric constant is larger than that of the imaginary part and agree very well with the empirical relations for both (ε_r & ε_i) as mentioned before. For the real part, there is a peak in the beginning of the curve and then there is a decrease (ε_r) at higher wavelength. The previously obtained data also agreed with n values which may be corresponding to the shift of the Fermi level within the conduction band and the increasing in carrier density. Also for the reasons mentioned before in section 4.6.2. It should be mentioned that the samples with S=0.04, and 0.02 have the highest and lowest ε_r, respectively, and the opposite versa for ε_i when increasing the wavelength.

5. Conclusion

Nanocomposites of sulphur-doped $Bi_2Te_{2.85}Se_{0.15}$ were prepared by the solvothermal method. Scanning electron microscopy analysis revealed the irregular and random shapes of the particles, which are in the order of a hundred nanometers. X-ray diffraction shows nearly single phase for the prepared samples and all of them were in the nanoscale, with more accurate dimensions than the obtained using SEM observations. Raman obtained phonon modes and TEM confirmed the data collected from XRD proving the nanostructure of samples. Seebeck results indicate that $Bi_2Te_{0.15}Se_{0.15}$ has the highest value (-108 μV/K) at 600 K. Moreover, while the best power factor was recorded for $Bi_2Te_{2.85}Se_{0.13}$ $S_{0.02}$ samples (1.3 x 10^{-2} mW/ K^2m at 600K). The optical energy gap was recorded in the range from 0.14 to 0.41ev indicating the sulphur effect on n- type $Bi_2Te_{2.85}Se_{0.15}$. The refractive index, as well as the extinction coefficient and the dielectric constants were influenced because of the difference of the ionic radii and the polarizability of S and Se. It can be concluded that the controlled dimensions of the prepared compositions, grain size and optical constants may have wide applications to be used in the future in energy conversion and optical data storage.

Acknowledgements

A. Sotelo acknowledges Gobierno de Aragón-FEDER (Research Group T 54-17R), and the Spanish MINECO-FEDER (Project MAT2017-82183-C3-1-R) for financial support.

References:

[1] G. Min, DM.Rowe, Cooling performance of integrated thermoelectric microcooler,Solid State Electron, 43(1999) 923–9: doi: 10.1016/S0038-1101(99)00045-3

[2] I. Stark and M. Stordeur, *18th International Conference on Thermoelectrics* (Baltimore, MD, USA, 1999), p. 465.

[3] TM. Tritt, Holey and Unholey Semiconductors, Science, 283 (1999) 804–5: doi: 10.1126/science.283.5403.804

[4] B. Fang, Z. Zeng, X. Yan and Z. Hu, Effects of annealing on thermoelectric properties of Sb_2Te_3 thin films prepared by radio frequency magnetron sputtering, J. Mater. Sci: Mater. Electron, 24,1105-1111 (2013): doi: 10.1007/s10854-012-0888-1

[5] Y. Jiang, Y. Y. Sun, M. Chen, Y. Wang, Z. Li, C. Song, K. He, L. Wang, X. Chen, Q. K. Xue, X. Ma and S. B. Zhang, Fermi-Level Tuning of Epitaxial Sb_2Te_3 Thin Films on Graphene by Regulating Intrinsic Defects and Substrate Transfer Doping, Phys. Rev. Lett., 108 (2012) 066809: dOI:https://doi.org/10.1103/PhysRevLett.108.066809

[6] E. Velmre, Thomas Johann Seebeck (1770–1831), Proc. Estonian Acad. Sci. Eng., 13(2007) 4, 276–282

[7] DC. Nemir, J.Beck, International Conference of Thermoelectric, Freiburg (2009).

[8] İ.Şişman, A. Başoğlu " Effect of Se content on the structural, morphological and optical properties of Bi2Te3_ySey thin films electrodeposited by under potential deposition technique" Materials Science in Semiconductor Processing 54(2016)57–64 :doi: http://dx.doi.org/10.1016/j.mssp.2016.07.001

[9] K. Biswas, J.Q.He, I.D.Blum, C.I.Wu,T.P.Hogan, D.N.Seidman, V.P.Dravid, M. G. Kanatzidis, High-performance bulk thermoelectrics with all-scale hierarchical architectures, Nature 489 (2012)414–418.

[10] Q.H. Zhang,X.Ai,L.J.Wang,Y.X.Chang,W.Luo,W.Jiang,L.D.Chen, Improved thermoelectric performance of silver nanoparticles-dispersed Bi2Te3 composites deriving from hierarchical two-phased heterostructure, Adv.Funct.Mater. 25(2015) 966–976.

[11] B. Ryu,B.-S.Kim,J.E.Lee,S.-J.Joo,B.-K.Min,H.W.Lee,S.Park,M.-W.Oh,Prediction of the band structures of Bi2Te3-related binary and Sb/Se-doped ternary thermoelectric materials, J.Korean Phys. Soc.68(2016)115–120.

[12] J. P. Carmo, J. F. Ribeiro, M. F. Goncalves and J. H. Correia, Thermoelectric generator and solid-state battery for stand-alone Microsystems, J.Micromech. Microeng.,20 (2010) 18: doi: https://doi.org/10.1088/0960-1317/20/8/085033

[13] W. Glatz, E. Schwyter, L. Durrer , C. Hierold, **Bi2Te3**-Based Flexible Micro Thermoelectric Generator With Optimized Design, J. Microelectromech. Syst., 18 (2009).763-772: doi: 10.1109/JMEMS.2009.2021104

[14] Z. Wang, B. Leonov, P. Fiorini ,C. V. Hoof, Realization of a wearable miniaturized thermoelectric generator for human body applications, Sens. Actuators A, 156 (2009) 95-102: doi: **https://doi.org/10.1016/j.sna.2009.02.028**

[15] M. Y. Kim and T. S. Oh, Thermoelectric Characteristics of the Thermopile Sensors with Variations of the Width and the Thickness of the Electrodeposited Bismuth-Telluride and Antimony-Telluride Thin Films, Mater. Trans., 51 (2010) 1909-1913: doi: **https://doi.org/10.2320/matertrans.M2010122**

[16] M. Y. Kim and T. S. Oh, Thermoelectric Thin Film Device of Cross-Plane Configuration Processed by Electrodeposition and Flip-Chip Bonding, Mater. Trans., 53 (2012) 2160-2165: doi: **https://doi.org/10.2320/matertrans.M2012265**

[17] D.K.C. MacDonald., Thermoelectricity: An Introduction to the Principles, Dover Publcation, Inc. (Book) (2006).

[18] P.H.Le, C.N. Liao, C.W. Luo, J.Y. Lin, J. Leu., Thermoelectric properties of bismuth-selenide films with controlled morphology and texture grown using pulsed laser deposition Appl. Surf. Sci, 285 (2013) 657: doi: **https://doi.org/10.1016/j.apsusc.2013.08.107**

[19] M. Takashiri, M. Takiishi, S. Tanaka, K. Miyazaki, and H. Tsukamoto., Thermoelectric properties of n-type nanocrystalline bismuth-telluride-based thin films deposited by flash evaporation, J. Appl. Phys., 101(2007) 074301 :doi: https://doi.org/10.1063/1.2717867
[20] K. Tezuka,S. KaseYue J. Shan, Syntheses of Bi2X3 (X = S, Se, Te) from elements under hydrothermal conditions,J. of Asian Cer. Socie., 2 (2014) 366-372 :doi: https://doi.org/10.1016/j.jascer.2014.07.009
[21] R.J. Mehta,Y.Zhang, C.Karthik,B. single,R.W Siegel, T. Borac, Tascinc,G.Ramanth, A new class of doped nanobulk high-figure-of-merit thermoelectrics by scalable bottom-up assembly, Nat. Mat. 11, (2012) 233-240:doi: 10.1038/nmat3213.
[22] A. Soni, Z.Yanynan, Y.Ligen, M.K.K. Aik, M.S. Dresselhans, Q. Xiong, Enhanced Thermoelectric Properties of Solution Grown Bi2Te3–xSex Nanoplatelet Composites, Nano. Letter, 12 (2012) 1203-1209: doi: https://doi.org/10.1021/nl2034859
[23] HJ. Goldsmid, Synthetic transverse thermoelements made from porous bismuth telluride and single crystal bismuth, Phy. Stat. Sol. A- Appl. and mater. Sci., 205 (2008) 2966-2969:doi: 10.1002/pssa.200824241
[24] D. Kim, C. Kim, HA D, et al. Fabrication and thermoelectric properties of crystal-aligned nano-structured Bi2Te3, Journal of Alloys and Compound 509 (17) (2011) 5211–5215.
[25] W.L. Ren, C.X. Cheng, Y.B. Xu, et al., Surfactant-assisted solvothermal synthesis of single-crystalline ternary Bi-Sb-Te hexagonal nanoplates, Journal of Alloys and Compound 501 (1) (2010) 120–123.
[26] D. Li, R.R. Sun, X.Y. Qin, Improving thermoelectric properties of p-type Bi2Te3-based alloys by spark plasma sintering, Progress in Natural Science:Materials International 21 (4) (2011) 336–340
[27] H. Scherrer, S. Scherrer,Thermoelectric properties of Bismuth Antimony telluride solid solution, in: D. M. Rowe, Thermoelectric Handbook: macro to nano, CRC Press, Taylor & Francis Group, 2006 ch27.
[28] H. Kaibe, Y. Tanaka, M. Sakata and I. Nishida, Anisotropic galvanomagnetic and thermoelectric properties of n-type Bi2Te3 single crystal with the composition of a useful thermoelectric cooling material, J. Phys. Chem. Solids, 50 (1989) 945-950: doi: https://doi.org/10.1016/0022-3697(89)90045-0
[29] F. Wu, H. Song , J. Jia , Xing Hu." Effects of Ce, Y, and Sm doping on the thermoelectric properties of Bi_2Te_3 alloy" Progress in Natural Science: Materials International, 2013, 23(4):408-412 : doi: http://dx.doi.org/10.1016/j.pnsc.2013.06.007
[30] K. Uemura and I. Nishida, Thermoelectric Semiconductor and Its Application, Nikkankogyo Shinbunsha, Tokyo, 1988 179.
[31] H. T. Kaibe, M. Sakata, Studies on the holes of p-TYPE $Bi_2Te_{2.85}Se_{0.15}$ single crystal I. A. Nishida, J. Phys. Chem. Solids, 51 (1990) 1083-1087: doi: https://doi.org/10.1016/0022-3697(90)90068-Q
[32] D. Perrin, M. Chitrob, S. Scherrer and H. Scherrer, Study of the n-type $Bi_2Te_{2.7}Se_{0.3}$ doped with bromine impurity, J. Phys. Chem. Solids, 61 (2000) 1687-1691: doi: https://doi.org/10.1016/S0022-3697(00)00030-5
[33] C. Liang, L. Liu, H. Li, D. Qian, C. Liu, J. Jia, J. Chen, Microstructural characterization of sulfur-doped Bi_2Te_3 crystals,Mate. Charac., 16 (2016) 172-178: doi: https://doi.org/10.1016/j.matchar.2016.02.009
[34] Y.L. Zhang, R.J. Mehta, M. Belley, L. Han, G. Ramanath, T. Borca-Tasciuc., Lattice thermal conductivity diminution and high thermoelectric power factor retention in nanoporous macroassemblies of sulfur-doped bismuth telluride nanocrystals, Appl. Phys. Lett., 100 (2012) 193113:doi: https://doi.org/10.1063/1.4711774
[35] R. Marschall, A. Mukherji, A. Tanksale, C. Sun, S.C. Smith, L. Wang, G.Q. Lu, Preparation of new sulfur-doped and sulfur/nitrogen co-doped $CsTaWO_6$ photocatalysts for hydrogen production from water under visible light, J. Mater. Chem., 21 (2011) 8871-8879:doi: 10.1039/C0JM02549F
[36] B. Ryu, B.-S.Kim, J.E.Lee, S.-J.Joo, B.-K.Min, H.W.Lee, S.Park,M.-W.Oh, Prediction of the band structures of Bi_2Te_3-related binary and Sb/Se-doped ternary thermoelectric materials, J.Korean Phys. Soc. 68 (2016) 115–120.
[37] Y.G.Wu, Z.J.Lin, Z.Y.Tian, C.Han,J.Liu, H.M.Zhang, Z.Q.Zhang, Z.C.Wang,L.C.Dai, Y.Cao,Z.Y.Hu, Fabrication of microstructured thermoelectric Bi_2Te_3 Thin Films by Seed Layer assisted Electrodeposition, Mater.Sci. Semicond. Process. 46(2016) 17–22.
[38] W.J. Xie, J. He, H.J. Kang, X.F. Tang, S. Zhu, M. Laver, S.Y. Wang, J.R.D. Copley, C.M. Brown, Q.J. Zhang, T.M. Tritt, Nano Letters 10 (2010) 3283–3289.

[39] B. Poudel, Q. Hao, Y. Ma, Y. Lan, A. Minnich, B. Yu, X. Yan, D. Wang, A. Muto, D. Vashaee, X. Chen, J. Liu, M.S. Dresselhaus, G. Chen, Z. Ren, Science 320 (2008) 634–638.
[40] R. D. Shannon, "Revised effective ionic radii and systematic studies of interatomic distances in halides and chalcogenides," *Acta Crystallographica* 32, no. 5 (1976): 751–767.
[41] A.L. Allred and E.G. Rochow, *J. Inorg. Nucl. Chem.*, 1958, 5, 264.
[42] X. Chen , L.Liu , Y. Dong, L.n Wang, L. Chen , W. Jianga " Preparation of nano-sized Bi2Te3 thermoelectric material powders by cryogenic grinding" Progress in Natural Science: Materials International, 2012,22(3):201-206
[43] 21J. G. Yu, H. T. Guo, S. A. Davis, and S. Mann, Adv. Funct. Mater 16, 2035–2041 (2006).
[44] R. Jin, J. Liu, G. Li," Facile solvothermal synthesis, growth mechanism and thermoelectric property of flower-like Bi_2Te_3"49(7), 460-466,2014**:doi:** https://doi.org/10.1002/crat.201400012
[45]. Deng, Y.; Nan, C.-W.; Wei, G.-D.; Guo, L.; Lin, Y.-H. Chem. Phys. Lett. 2003, 374, 410.
[46]. Zhao, X. B.; Ji, X. H.; Zhang, Y. H.; Cao, G. S.; Tu, J. P. Appl. Phys. A 2005, 80, 1567.
[47]. Fan, X. A.; Yang, J. Y.; Xie, Z.; Li, K.; Zhu, W.; Duan, X. K.; Xiao, C. J.; Zhang, Q. Q. J. Phys. D: Appl. Phys. 2007, 40, 5975.
[48] Hee Jin Kim, Mi-Kyung Han, Ha-young Kim, Wooyoung Lee, and Sung-Jin Kim" Morphology Controlled Synthesis of Nanostructured Bi2Te3" Bull. Korean Chem. Soc. 2012, Vol. 33, No. 12 3977 Doi: http://dx.doi.org/10.5012/bkcs.2012.33.12.3977
[49] Fang Wua,, Wei Wang , Xing Hu , Mingsheng Tang" Thermoelectric properties of I-doped n-type Bi_2Te_3-based material prepared by hydrothermal and subsequent hot pressing 27,(2017),203-207 : doi: **http://dx.doi.org/10.1016/j.pnsc.2017.02.009**
[50] Z.H. Zheng, P. Fan, T.B. Chen, Z.K. Cai, P.J. Liu, G.X. Liang, D.P. Zhang, X.M. Cai, Thin Solid Films, 520 5245–5248 (2012):doi: **10.1016/j.tsf.2012.03.086**
[51] D. Park, S. Park, K. Jeong, H. Jeong, J. Yong Song, M. Cho, Thermal and Electrical Conduction of Single-crystal Bi_2Te_3 Nanostructures grown using a one step process, Scientific reports, 6 (2016) 19132: doi: https://doi.org/10.1038/srep19132
[52] C. Wang, X. Zhu, L. Nilsson, J. Wen, G. Wang, X. Shan,Q. Zhang, S. Zhang, J. Jia and Q. Xue, In situ Raman spectroscopy of topological insulator Bi_2Te_3 films with varying thickness, Nano Res., 6 (2013) 688–692: doi: **10.1007/s12274-013-0344-4**
[53] G. D. Keskar, R. Podila, L. Zhang, A. M. Rao, and L.D. Pfefferle, Synthesis and Raman Spectroscopy of Multiphasic Nanostructured Bi–Te Networks with Tailored Composition, J. Phys. Chem. C, 117 (2013). 9446−9455 :doi: **https://doi.org/10.1021/jp402879h**
[54] H. Xu, Y. Song, Q. Gong, W. Pan, X. Wu and S. Wang, Raman spectroscopy of epitaxial topological insulator Bi_2Te_3 thin films on GaN substrates, Modern Physics Letters B, 29(15) 1550075 (10 pages) (2015): doi: **https://doi.org/10.1142/S021798491550075X**
[55] N. S. Abishek, and K. Gopalakrishna Naik, Influence of gamma ray irradiation on stoichiometry of hydrothermally synthesized bismuth telluride nanoparticles,AIP Conference Proceedings 1953 (2018) 030067: doi: **https://doi.org/10.1063/1.5032402**
[56] V. Russo, A. Bailini, M. Zamboni, M. Passoni, C. Conti, C.S. Casari, A. LiBassi, C.E. Bottani, Raman spectroscopy of Bi-Te thin films, J. Raman Spectrosc., 39 205 (2008): doi: **https://doi.org/10.1002/jrs.1874**
[57] D. Mei, H. Wang, Y. Li, Z. Yao, T. Zhu, Microstructure and thermoelectric properties of porous $Bi_2Te_{2.85}Se_{0.15}$ bulk materials fabricated by semisolid powder processin, J. Mater. Res., 30 (2015) 2585-2592: doi: **https://doi.org/10.1557/jmr.2015.142**
[58] W.S. Liu, X. Yan, G. Chen, Z.F. Ren, Nano Energy 1 (2012) 42–56
[59] J.R.Sambles,Thin soild films 106,321,(1983).
[60] A.F. Mayadas and M. shatzkes, phys. Rev B 1,1382 (1970).
[61] J.W.C. Devries, Thin solid films 167,25 (1988).
[62] Z. Wang, K. Matsuoka, T. Araki, T. Akao, T. Onda and Z. Chen, Extrusion Behavior and Thermoelectric Properties of $Bi_2Te_{2.85}Se_{0.15}$ Thermoelectric Materials, Procedia Engineering , 81 (2014) 616 – 621.doi: **10.1016/j.proeng.2014.10.049**
[63] Fang Wua,b , Hongzhang Songa , Jianfeng Jiaa , Xing Hua "Effects of Ce, Y, and Sm doping on the thermoelectric properties of Bi_2Te_3 alloy" Progress in Natural Science: Materials International, 2013,23(4):408-412: Doi: **http://dx.doi.org/10.1016/j.pnsc.2013.06.007**
[64] Min Hong, Thomas C. Chasapis, Zhi-Gang Chen, Lei Yang, Mercouri G. Kanatzidis, G. Jeffrey Snyderand Jin Zou" n-Type Bi2Te3-xSex Nanoplates with Enhanced Thermoelectric Efficiency Driven by Wide-Frequency Phonon Scatterings and Synergistic Carrier Scatterings "ACS Nano 2016, 10, 4, 4719-4727 : doi : **https://doi.org/10.1021/acsnano.6b01156**

[65] W.Jung, H. Kim, and I.Kim, Charge Transport and Thermoelectric Properties of N-type $Bi_{2-x}Sb_xTe_{3-y}Se_y:I_m$ Prepared by Encapsulated Melting and Hot Pressing Korean J. Met. Mater., 56 (2018) 544-550: doi: **https://doi.org/10.3365/KJMM.2018.56.7.544**

[66] M. Fusa, N. Sumida and K. Hasezaki, Preparation of *n*-Type $Bi_2Te_{2.85}Se_{0.15}$ Thermoelectric Semiconductor without Harmful Dopants, Materials Transactions, 53 (2012) 597- 600:doi: **https://doi.org/10.2320/matertrans.ME201108**

[67] J. Jiang , L. D. Chen, S. Q. Bai, Q. Yao, Q. Wang, Thermoelectric properties of textured p-type $(Bi,Sb)_2Te_3$ fabricated by spark plasma sintering,Scr. Mater., 52 (2005) 347-351: doi: **https://doi.org/10.1016/j.scriptamat.2004.10.038**

[68] S. Wang, W. Xic, H. Li, X. Tang, Enhanced performances of melt spun $Bi_2(Te,Se)_3$ for n-type thermoelectric legs, Intermetallics, 19 (2011) 1024-1031: doi: **https://doi.org/10.1016/j.intermet.2011.03.006**

[69] H. S. Kim, Z.M. Gibbs, Y. Tang, H. Wang, G.J. Snyder, Characterization of Lorenz number with Seebeck coefficient measurement, APL Materials, 3 (2015) 041506 :doi: **https://doi.org/10.1063/1.4908244**

[70] X. A. Fan, J. Y. Yang, W. Zhu, S. Q. Bao, X. K. Duan, C. J. Xiao, K. Li, Preferential orientation and thermoelectric properties of n-type $Bi_2Te_{2.85}Se_{0.15}$ alloys by mechanical alloying and equal channel angular extrusion, J. Phys. D: Appl. Phys. 40 (2007)5727–5732:doi: **https://doi.org/10.1088/0022-3727/40/18/033**

[71] P. Kubelka, New contributions to the optics of intensely light-scattering materials. Part I, Josa 38(5) (1948) 448-457.

[72] F. Yakuphanoglu, R. Mehrotra, A. Gupta, M. Munoz, J Appl Polymer Sci 114, 794 (2009))

[73] E. Yassitepe, Z. Khalifa, G.H. Jaffari, C.-S.Chou, S. Zulfiqar, M.I.Sarwar, S.I. Shah, Powder Technology 201, 27 (2010)

[74] J. Tauc, A.Menth, States in the gap, J.Non-Cryst. Solids 8–10 (1972) 569–585.

[75] F. Yakuphanoglu, J Alloys Compd 507, 184 (2010)

[76] C.B.Satterhwaite, R.W.UreJr, *"Electrical and Thermal Properties of BifTe",* Phys. Rev. B: Condens. Matter ., 108 (1957) 1164.

[77] Kojihayashi, D.Koto, K.Shimakawa, *"Photoinduced effects in amorphous chalcogenide films by vacuum ultra-violet light",* J.Non-Cryst.Solids, 198 (1996) 696.

[78] A.Akrap,A.Ubaldini, E.Giannini, L.Forro, $Bi_2Te_{3-x}Se_x$ series studied by resistivity and thermopower, EPL-Euro phys. Lett.107(2014)57008.

[79] A.Sharma, P.B.Barman, An optical study of vacuum evaporated amorphous $Ge_{20}Te_{80-x}Bi_x$ thin films using transmission and reflection spectra,Appl.Phys.B97 (2009)835–840.

[80] A.Sharma, P.B.Barman, An optical study of vacuum evaporated $Se_{85-x}Te_{15}Bi_x$ chalcogenides thin films, Physica B 405 (2010)822–827.

[81] . Aicha.A.R.Elshabini-Riad, Fred. D.Barlow, "*Thin film technology handbook",* McGraw-Hill, New York, (1997).

[82] . H.Brooks, "*Advances in Electronics and Electron Physics",* Academic Press, New York,(1955).

[83] M. Caglar, F.Yakuphanoglu, Structural and optical properties of copper doped ZnO films derived by sol–gel, Appl. Surf. Sci. 258(2012)3039–3044.

[84] S.R. Elliott,The Physics and Chemistry of Solids, Wiley,Chichester,2000.

[85] N.A. Subrahamanyam, A textbook of optics, 9 thedn.(Brj Laboratory, Delhi, 1977).

[86] S. Ilican, Y. Caglar, M. Caglar, F. Yakuphanoglu, Appl Surf Sci255, 2353 (2008).

[87] S.A. Fayek,S.M.El-Sayed,Optical properties of amorphous Ge_{28-x} $Se_{72}Sb_x$ thin films, NDTE Int.39(2006) 39–44.

Tables:

Table 1**:** Lattice parameters, Grain size and Strain calculated from the highest intense crystalline peak

Sample	Lattice parameters		Grain Size(nm)	Strain $x10^{-3}$	E_g (ev)
	a (Å)	c (Å)			
$Bi_2Te_{2.85}Se_{0.015}$	4.52	28.81	21	4.7	0.23
$Bi_2Te_{2.85}Se_{0.13}S_{0.02}$	4.56	28.97	17.5	7.0	0.33
$Bi_2Te_{2.85}Se_{0.11}S_{0.04}$	4.55	28.88	24	4.5	0.14
$Bi_2Te_{2.85}Se_{0.09}S_{0.06}$	4.56	28.90	18	7.6	0.41

Table 2: Frequency of Raman peaks of $Bi_2Te_{2.85}Se_{0.15-x}S_x$ in the present study and the literature.

Ref [28]	Ref [31]	Ref [32]	Ref [33]	$Bi_2Te_{2.85}Se_{0.15}$	$Bi_2Te_{2.85}Se_{0.13}S_{0.02}$	$Bi_2Te_{2.85}Se_{0.11}S_{0.04}$	$Bi_2Te_{2.85}Se_{0.09}S_{0.06}$
	86.7		90	--	--	--	84.892
	99.6	99	102	94.035	92.063	93.81	97.56
122	115.4	114/ 116	115/ 120	119.98	113.42	122.41	113.34
134	131.7	134/1 42	135	141.72	139.44	144.09	139.41
				184.52	180.28	172.36	178.11
758				756.31	756.18	756.2	756.53

Fig 1 Energy – dispersive X-ray spectra for :(a) $Bi_2Te_{2.85}Se_{0.15}$ & (b) $Bi_2Te_{2.85}Se_{0.13}S_{0.02}$

Fig 2 a) SEM image, b) surface particle size for $Bi_2Te_{2.85}Se_{0.15}$, c,d & e) The elemental distribution mapping for Te, Se and Bi respectively

Fig 3 XRD diffractogrames for $Bi_2Te_{2.85}Se_{0.15}S_{0.15-x}$ (x=0.0, 0.02, 0.04 and 0.06

Fig 4 The deconvolution analysis using Winfit program for the maximum intensity peak for: **a)** $Bi_2Te_{2.85}Se_{0.015}$ & **b)** $Bi_2Te_{2.85}Se_{0.09}S_{0.06}$ respectively

Fig 5 The unit cell volume versus the (S) concentration into $Bi_2Te_{2.85}Se_{0.15-x}S_x$

Fig 6 Raman spectra recorded for $Bi_2Te_{2.85}Se_{0.15-x}S_x$ samples

Fig 7 FWHM of Raman phonon modes of $Bi_2Te_{2.85}Se_{0.15-x}S_x$ as a function of S concentrations

Fig 8 Seebeck coefficient (S) temperature dependence for $Bi_2Te_{2.85}Se_{0.15-x}S_x$ (x=0.0, 0.02, 0.04 and 0.06)

Fig 9 Electrical resistivity Temperature dependence for $Bi_2Te_{2.85}Se_{0.15-x}S_x$ (x=0.0, 0.02, 0.04 and 0.06)

Fig 10 Temperature dependence of the power factor of $Bi_2Te_{2.85}Se_{0.15-x}S_x$ (x=0.0, 0.02, 0.04 and 0.06)

Fig 11 Temperature dependence of Electronic Thermal conductivity of $Bi_2Te_{2.85}Se_{0.15-x}S_x$ (x=0.0, 0.02, 0.04 and 0.06)

Fig 12 Fitted Raman spectrum pattern for $Bi_2Te_{2.85}Se_{0.09}S_{0.06}$ with 50*50 μm^2 laser spot size

Fig 13 Fitted Raman spectrum pattern for $Bi_2Te_{2.85}Se_{0.09}S_{0.06}$ with 50*50 μm^2 laser spot

Fig 14 $(\alpha\ \mathbf{h\upsilon})^{1/2}$ versus photon energy curves for $Bi_2Te_{2.85}Se_{0.15-x}S_x$ samples.

Fig.15 Variation of refractive index with wavelength for $Bi_2Te_{2.85}Se_{0.15-x}S_x$ samples.

Fig 16 Variation of extinction coefficient for $Bi_2Te_{2.85}Se_{0.15-x}S_x$ samples, as a function of wavelength.

Fig 17 (a) Real and (b) imaginary parts of the dielectric spectra for $Bi_2Te_{2.85}Se_{0.15-x}S_x$ samples.

Figure 1

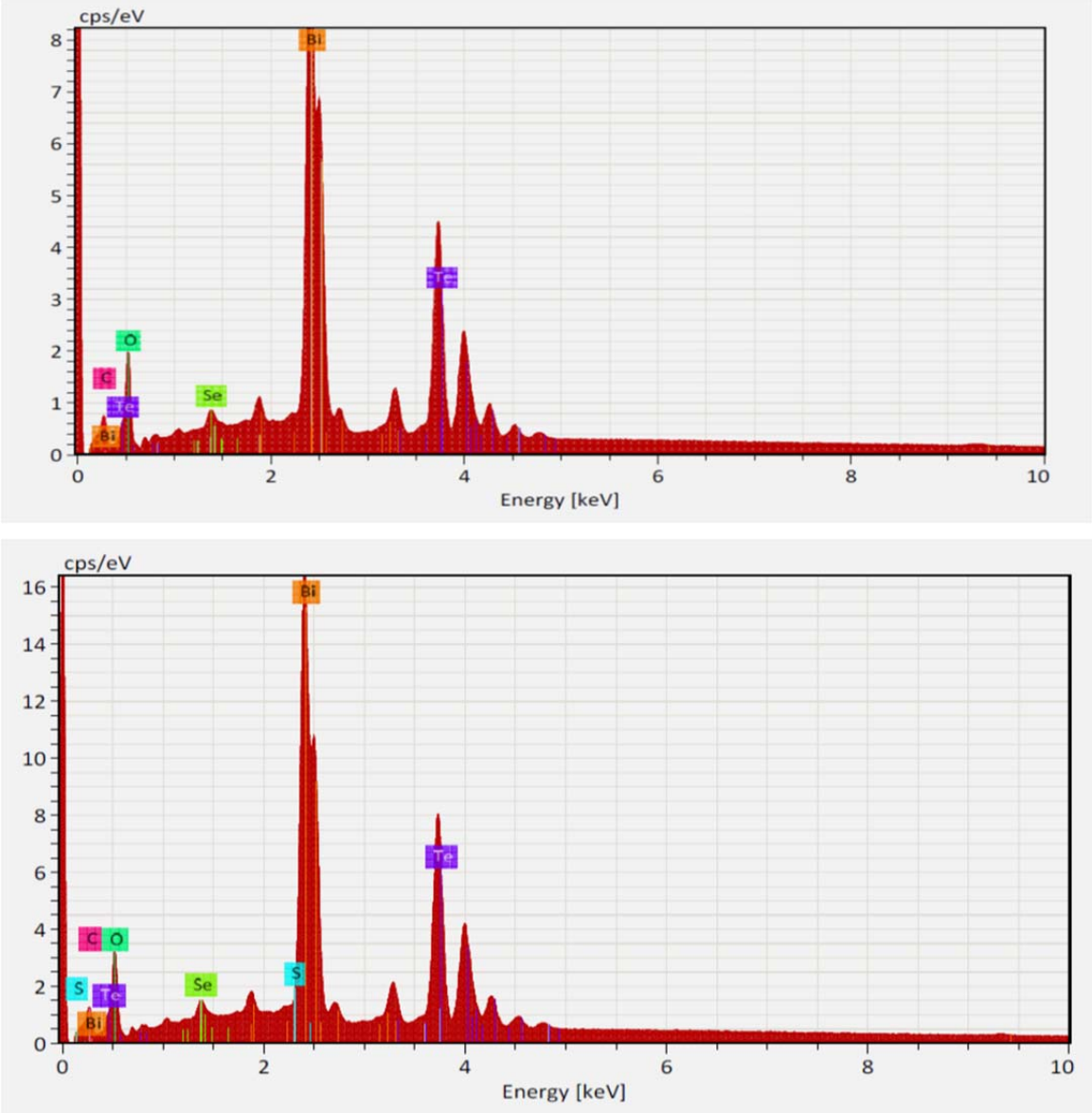
cps/eV
Bi
Te
O
C
Se
Bi
Energy [keV]
cps/eV
Bi
Te
C
O
S
Te
Bi
Se
S
Energy [keV]

Figure 2

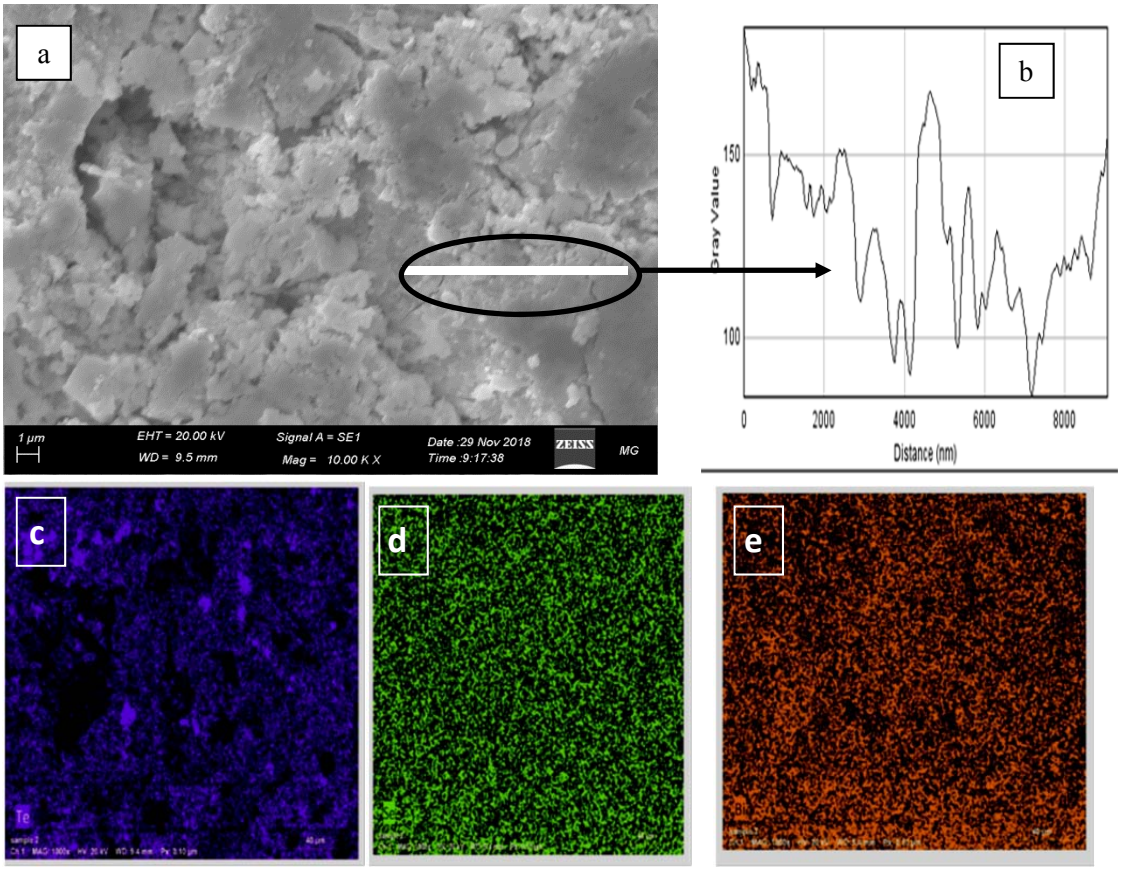
a
1 µm
EHT = 20.00 kV
WD = 9.5 mm
Signal A = SE1
Mag = 10.00 K X
Date :29 Nov 2018
Time :9:17:38
ZEISS
MG
b
Gray Value
150
100
0
2000
4000
6000
8000
Distance (nm)
c
Te
d
e

Figure 3

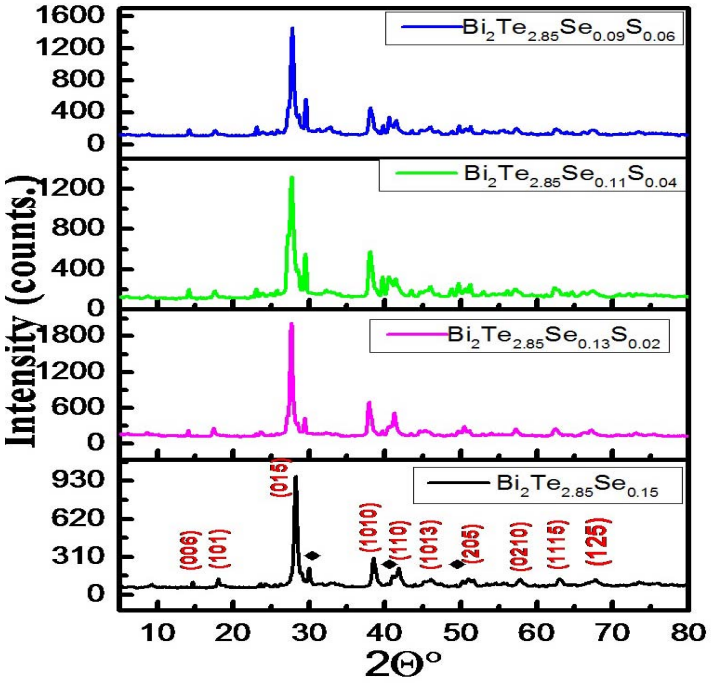
Bi2Te2.85Se0.09S0.06
Bi2Te2.85Se0.11S0.04
Bi2Te2.85Se0.13S0.02
Bi2Te2.85Se0.15
Intensity (counts.)
2Θ°
(006)
(101)
(015)
(1010)
(110)
(1013)
(205)
(0210)
(1115)
(125)

Figure 4

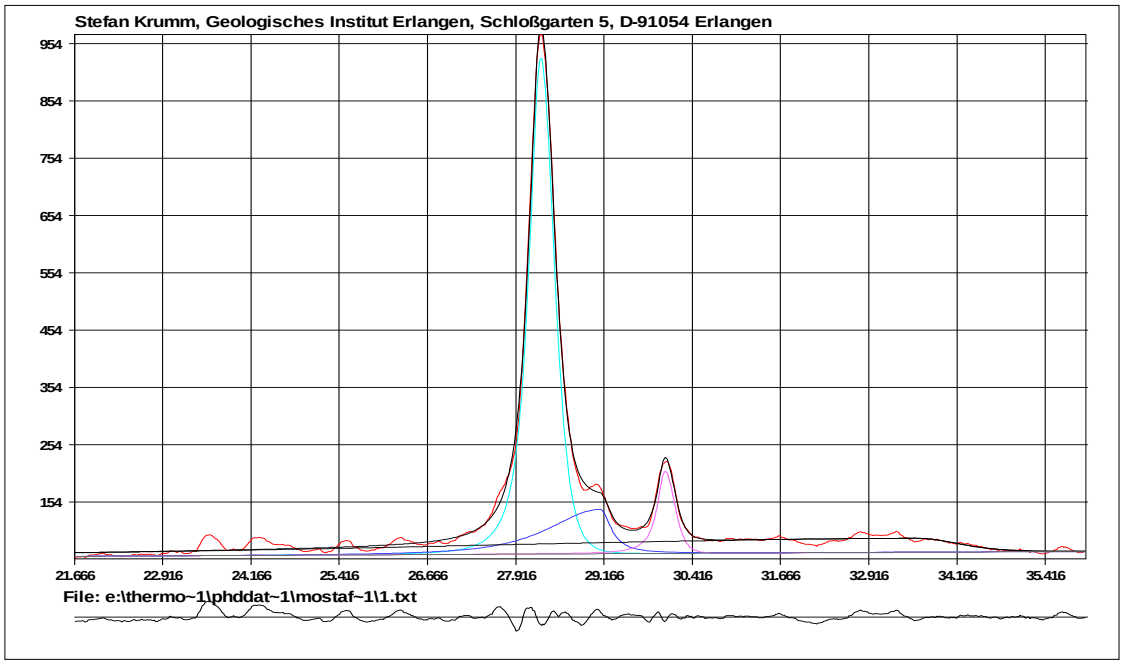
Stefan Krumm, Geologisches Institut Erlangen, Schloßgarten 5, D-91054 Erlangen
954
854
754
654
554
454
354
254
154
21.666
22.916
24.166
25.416
26.666
27.916
29.166
30.416
31.666
32.916
34.166
35.416
File: e:\thermo~1\phddat~1\mostaf~1\1.txt

Figure 5

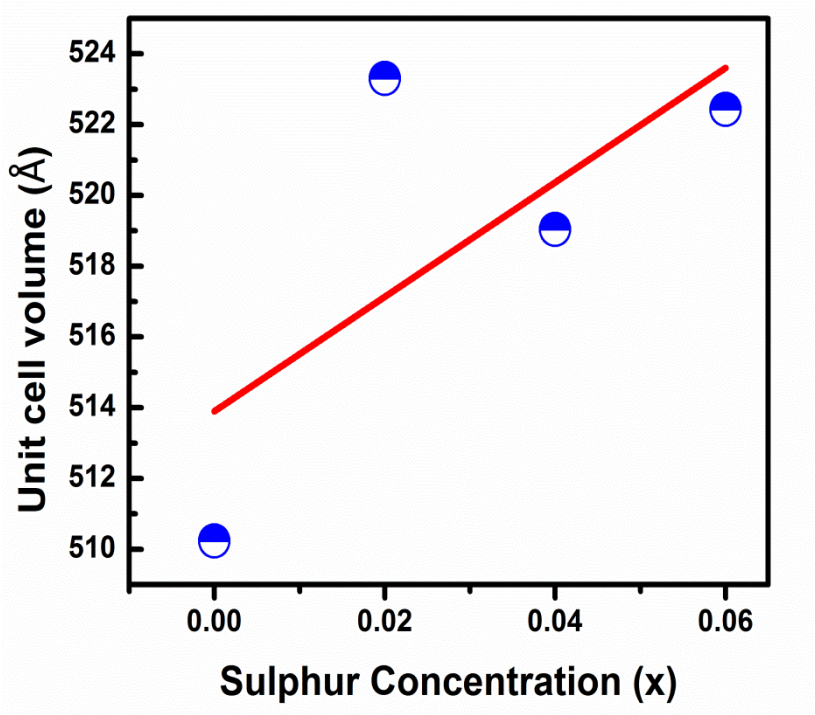
Unit cell volume (Å)
524
522
520
518
516
514
512
510
0.00
0.02
0.04
0.06
Sulphur Concentration (x)

Figure 6

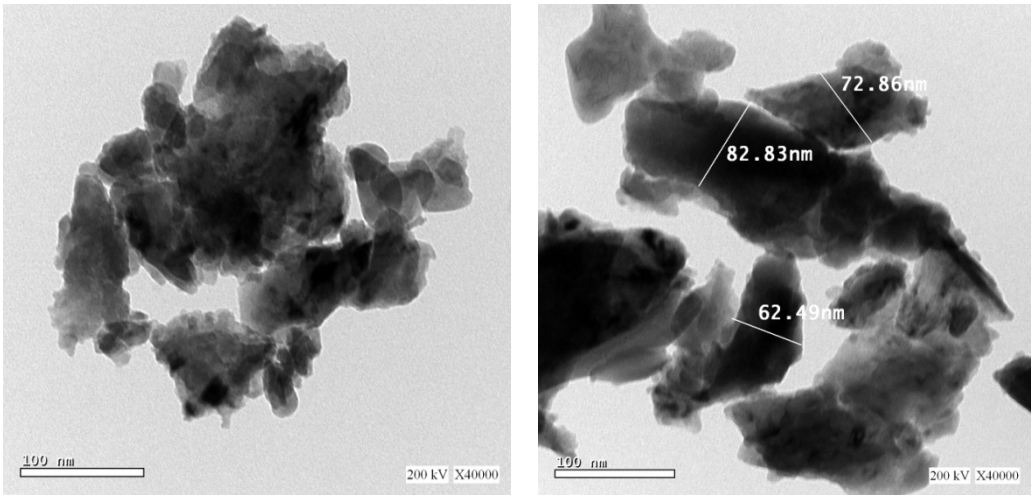
100 nm
200 kV X40000
72.86nm
82.83nm
62.49nm
100 nm
200 kV X40000

Figure 7

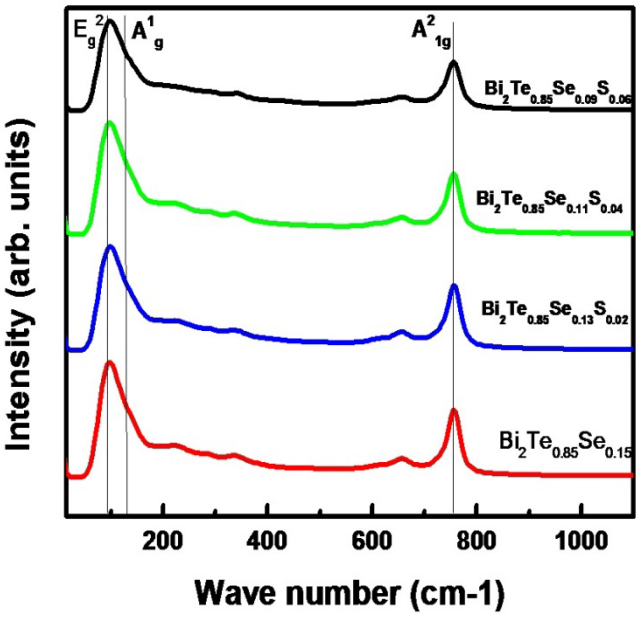
E_g^2
A^1_g
A^2_{1g}
$Bi_2Te_{0.85}Se_{0.09}S_{0.06}$
$Bi_2Te_{0.85}Se_{0.11}S_{0.04}$
$Bi_2Te_{0.85}Se_{0.13}S_{0.02}$
$Bi_2Te_{0.85}Se_{0.15}$
Intensity (arb. units)
200
400
600
800
1000
Wave number (cm-1)

Figure 8

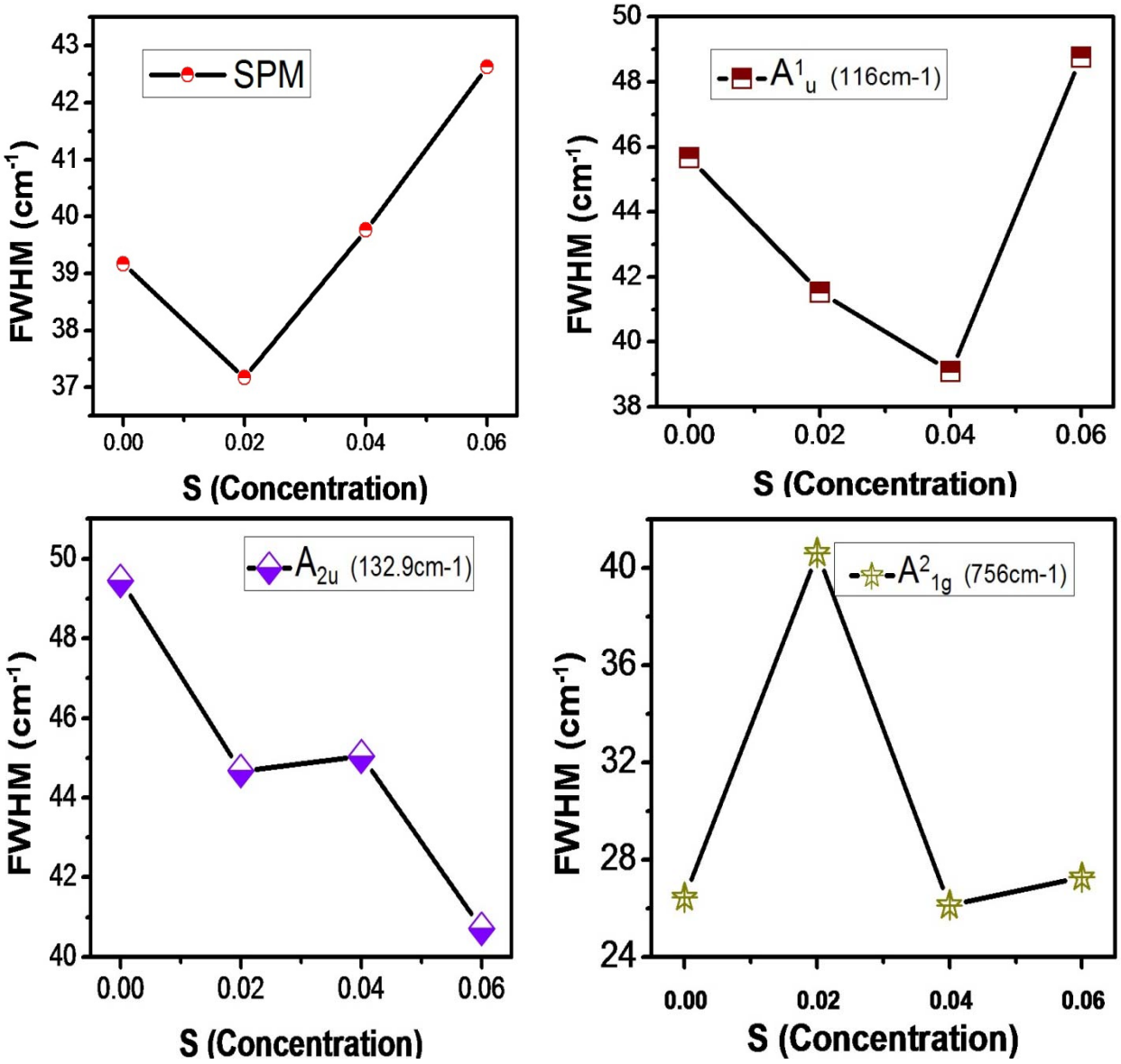
SPM
FWHM (cm-1)
S (Concentration)
A1u (116cm-1)
A2u (132.9cm-1)
A2 1g (756cm-1)

Figure 9

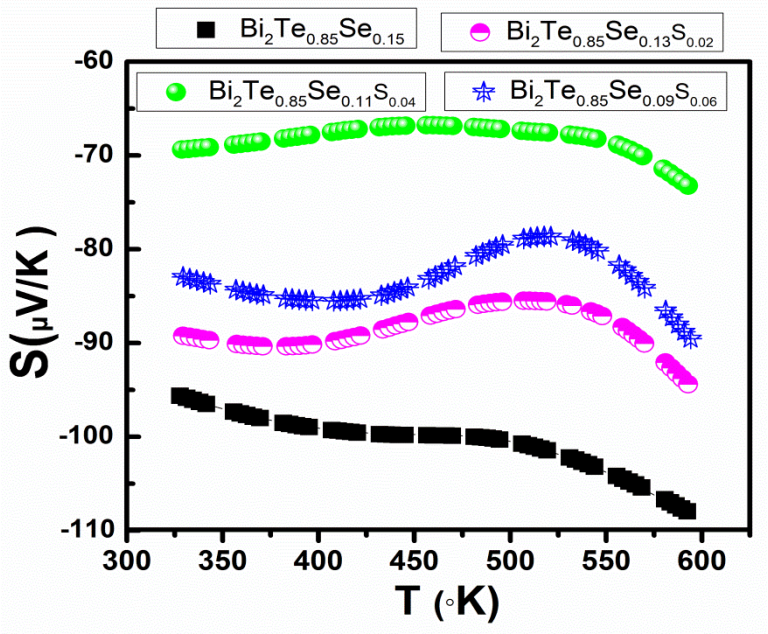
Bi2Te0.85Se0.15
Bi2Te0.85Se0.13S0.02
Bi2Te0.85Se0.11S0.04
Bi2Te0.85Se0.09S0.06
-60
-70
-80
-90
-100
-110
S(μV/K)
300
350
400
450
500
550
600
T (◦K)

Figure 10

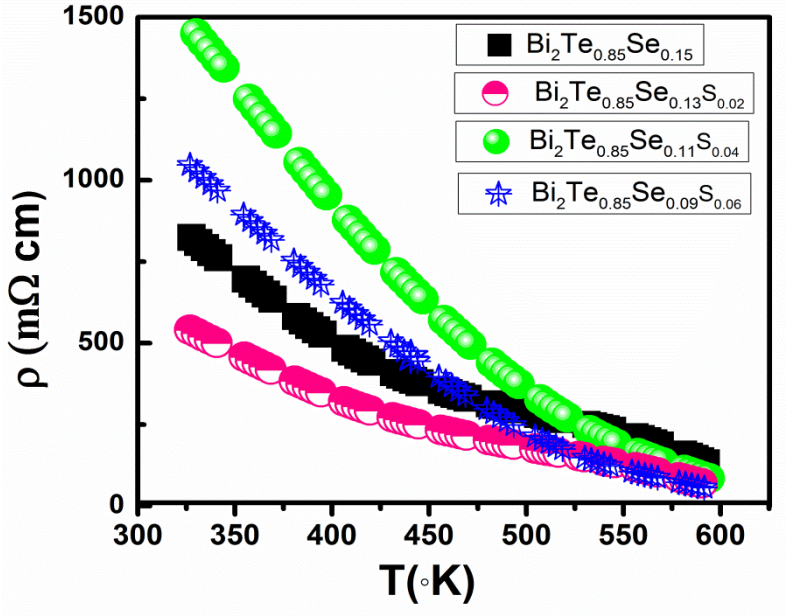
1500
1000
500
0
300
350
400
450
500
550
600
ρ (mΩ cm)
T(◦K)
Bi2Te0.85Se0.15
Bi2Te0.85Se0.13S0.02
Bi2Te0.85Se0.11S0.04
Bi2Te0.85Se0.09S0.06

Figure 11

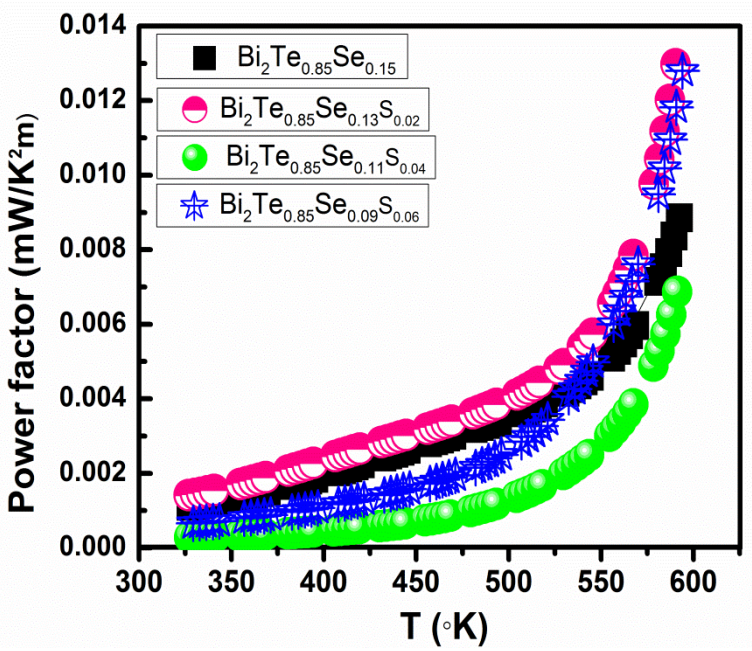
Bi2Te0.85Se0.15
Bi2Te0.85Se0.13S0.02
Bi2Te0.85Se0.11S0.04
Bi2Te0.85Se0.09S0.06
Power factor (mW/K²m)
0.014
0.012
0.010
0.008
0.006
0.004
0.002
0.000
300
350
400
450
500
550
600
T (◦K)

Figure 12

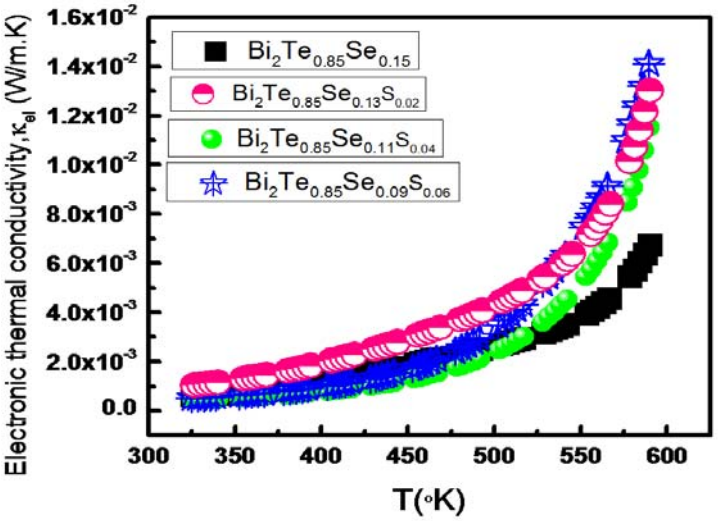
Electronic thermal conductivity, κ_{el} (W/m.K)
1.6x10^{-2}
1.4x10^{-2}
1.2x10^{-2}
1.0x10^{-2}
8.0x10^{-3}
6.0x10^{-3}
4.0x10^{-3}
2.0x10^{-3}
0.0
300
350
400
450
500
550
600
T(°K)
$Bi_2Te_{0.85}Se_{0.15}$
$Bi_2Te_{0.85}Se_{0.13}S_{0.02}$
$Bi_2Te_{0.85}Se_{0.11}S_{0.04}$
$Bi_2Te_{0.85}Se_{0.09}S_{0.06}$

Figure 13

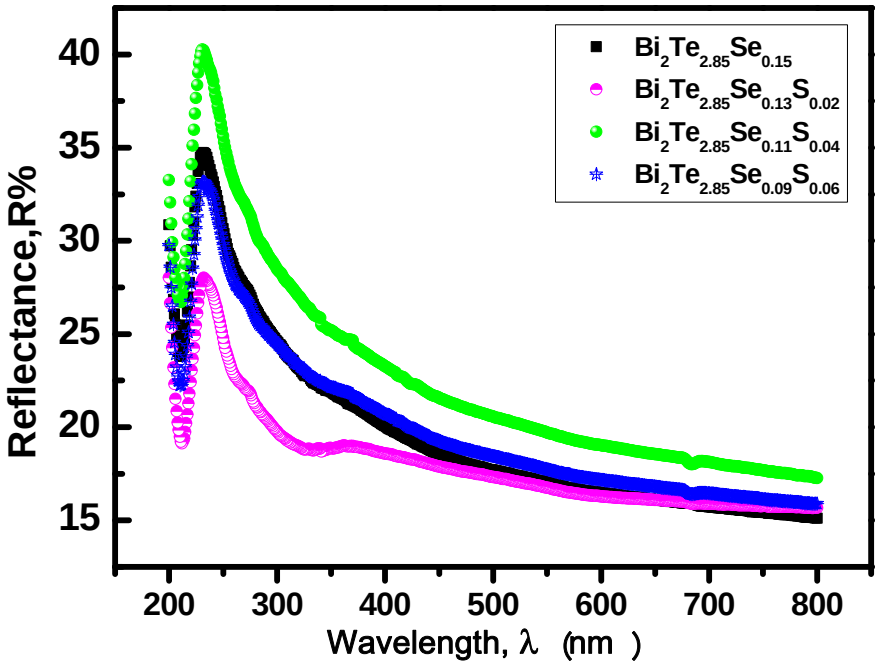
Reflectance,R%
40
35
30
25
20
15
200
300
400
500
600
700
800
Wavelength, λ (nm)
Bi2Te2.85Se0.15
Bi2Te2.85Se0.13S0.02
Bi2Te2.85Se0.11S0.04
Bi2Te2.85Se0.09S0.06

Figure 14

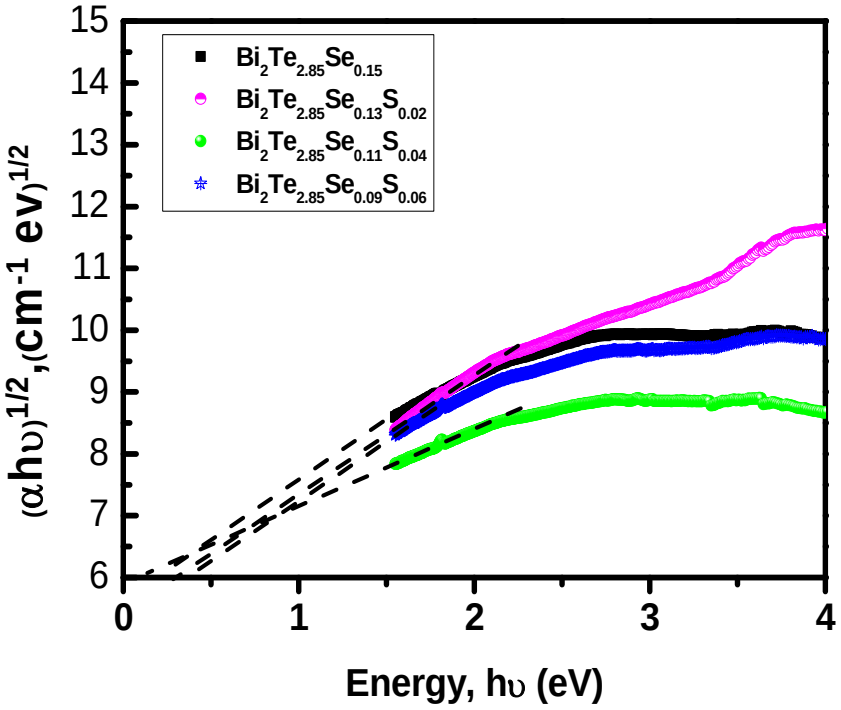
Bi2Te2.85Se0.15
Bi2Te2.85Se0.13S0.02
Bi2Te2.85Se0.11S0.04
Bi2Te2.85Se0.09S0.06
(αhυ)1/2,(cm-1 eV)1/2
Energy, hυ (eV)
15
14
13
12
11
10
9
8
7
6
0
1
2
3
4

Figure 15

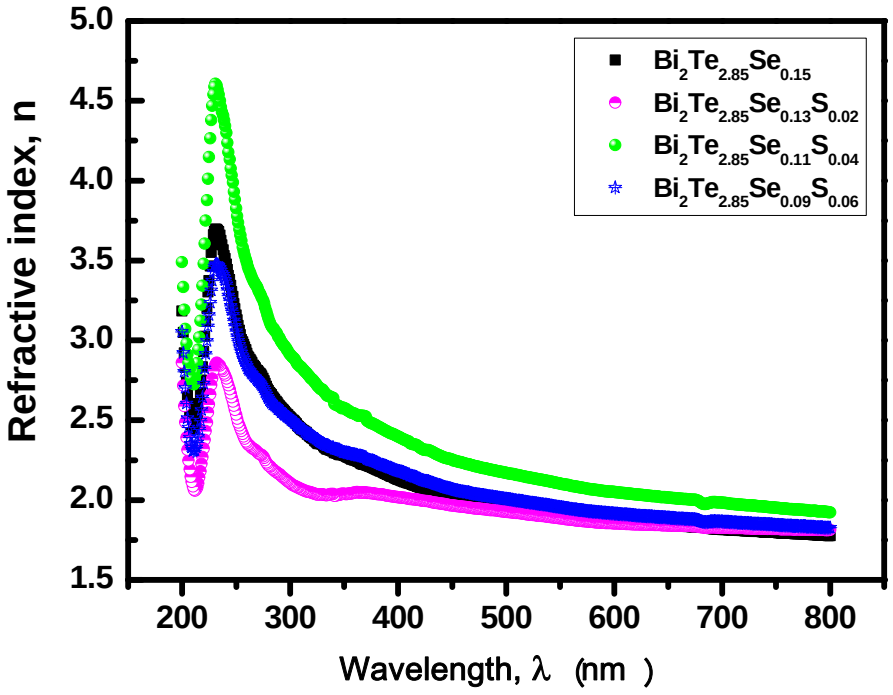
Refractive index, n
Wavelength, λ (nm)
5.0
4.5
4.0
3.5
3.0
2.5
2.0
1.5
200
300
400
500
600
700
800
Bi2Te2.85Se0.15
Bi2Te2.85Se0.13S0.02
Bi2Te2.85Se0.11S0.04
Bi2Te2.85Se0.09S0.06

Figure 16

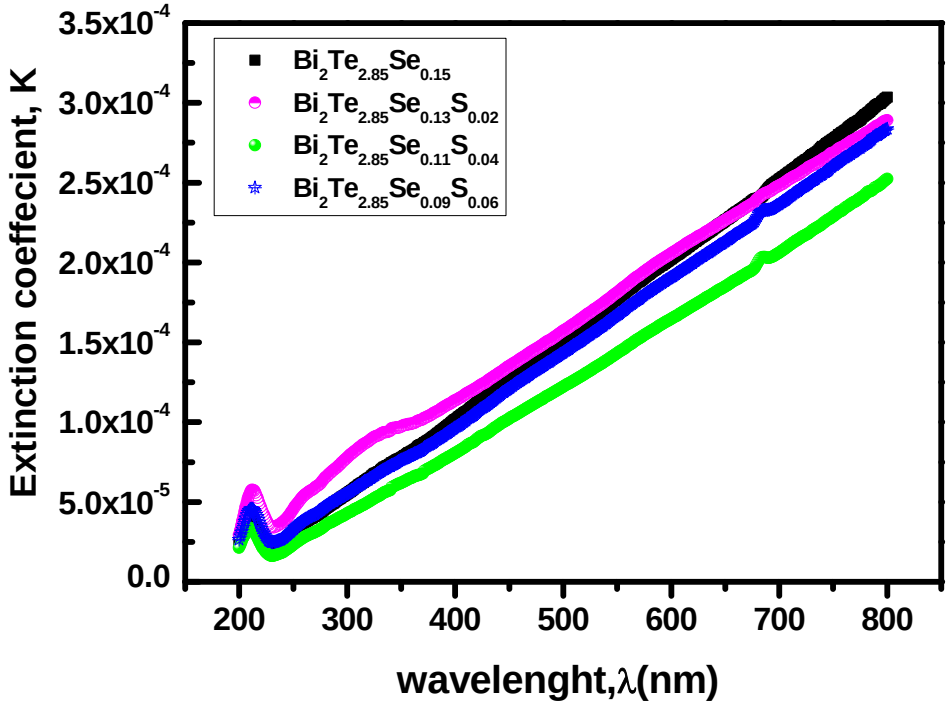
Extinction coeffecient, K
3.5x10-4
3.0x10-4
2.5x10-4
2.0x10-4
1.5x10-4
1.0x10-4
5.0x10-5
0.0
200
300
400
500
600
700
800
wavelenght,λ(nm)
Bi2Te2.85Se0.15
Bi2Te2.85Se0.13S0.02
Bi2Te2.85Se0.11S0.04
Bi2Te2.85Se0.09S0.06

Figure 17

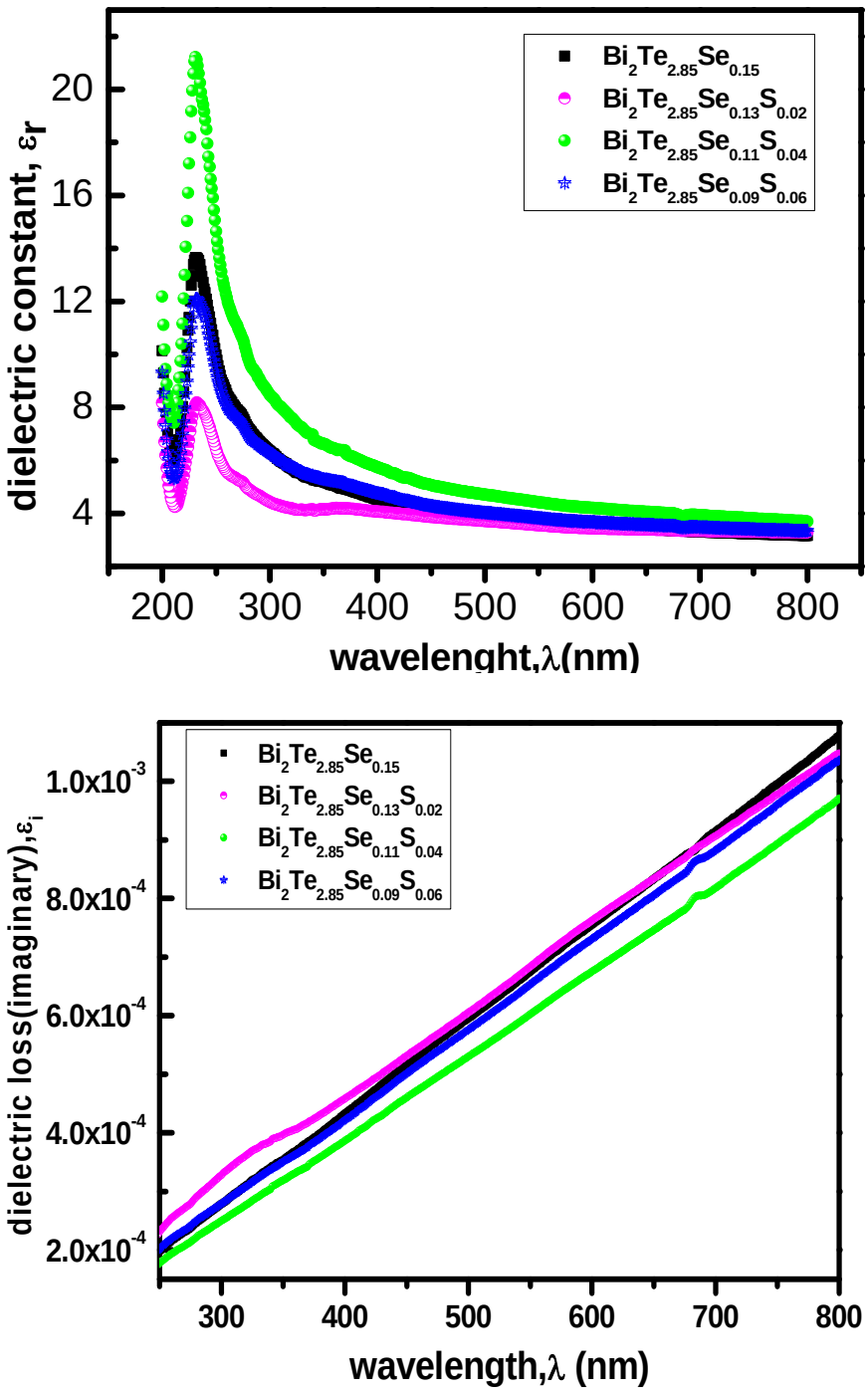
dielectric constant, ε_r
wavelenght,λ(nm)
$Bi_2Te_{2.85}Se_{0.15}$
$Bi_2Te_{2.85}Se_{0.13}S_{0.02}$
$Bi_2Te_{2.85}Se_{0.11}S_{0.04}$
$Bi_2Te_{2.85}Se_{0.09}S_{0.06}$
dielectric loss(imaginary),ε_i
wavelength,λ (nm)